A Comparative Study of Constitutive Characteristics and Microstructure Evolution between Uniaxial and Plane Strain Compression of an AA6061 Alloy

Fangcheng Qin, Huiping Qi, and Yongtang Li

The hot deformation behavior of an AA6061 alloy was comparatively studied by uniaxial compression (UC) and plane strain compression (PSC) in the temperature range of 300-450 °C and strain rate range of 0.01-5 s^{-1}. The processing maps were constructed based on a dynamic materials model, and the associated microstructures were observed. Under the same deformation conditions, the flow stress of the AA6061 alloy during PSC is higher than that during UC, which can be characterized by the Zener–Hollomon (Z) parameter in a hyperbolic sine-type equation with an activation energy Q of 175.2 kJ mol^{-1} and 201.9 kJ mol^{-1}, respectively. In addition, the instability domain is narrower under PSC compared to that under UC. The observed microstructures also indicate that as the Z value decreases, the tendency of dynamic recrystallization increases during PSC. The softening mechanisms in the AA6061 alloy after PSC and UC mainly consist of the dynamic recovery that is accompanied by a slight dynamic recrystallization. The optimum parameters are in the temperature range of 360-450 °C and strain rate range of 0.03-0.3 s^{-1} for UC, and for PSC, the optimum parameters are in the temperature range of 320-400 °C and strain rate range of 0.01-0.05 s^{-1}.

1. Introduction

The AA6061 alloy is a precipitation-hardenable Al-Mg-Si alloy containing magnesium and silicon as the main alloying elements (Ref 1, 2). Due to their excellent properties, such as high specific strength, excellent corrosion resistance and acceptable weldability, AA6061 products, such as rings, are widely used, especially as critical components in the aircraft, automobile and wind power industries (Ref 3-6). To enhance the workability and obtain excellent performance in AA6061 ring components, the deformation parameters, including the temperature, strain rate and strain, should be accurately controlled under specified conditions.

Hot ring rolling (HRR) is an advanced incremental forming technique to fabricate ring products (Ref 7, 8). The ring blank thickness is gradually reduced with a progressively narrowing gap between the driving roll and the idle roll during HRR, and the final height of the ring is controlled by the axial rolls (Ref 9). Under the action of the driving roll and friction, the ring blank is subjected to an extra shear deformation in addition to the compression in the surface layers. Thus, the ring blank experiences complicated stress and strain states, which results in dynamic responses, and microstructures after HRR are different from those after hot forging (Ref 4, 10, 11). Previous research (Ref 12-14) found that plane strain compression (PSC) is a valuable method for clarifying the microstructure evolution mechanism and simulating the HRR condition. Until now, many research efforts have concentrated on the deformation behavior and the constitutive model of the AA6061 alloy in uniaxial compression (UC) (Ref 1, 15, 16), but studies of those in the PSC condition are insufficient. Ezatpour et al. (Ref 1) established the constitutive models and processing maps for a 6061-T6 alloy by UC tests and found that the microstructure evolution mechanisms transformed from dynamic recovery (DRV) to dynamic recrystallization (DRX) with increasing temperature and decreasing strain rate. Dorbane et al. (Ref 17) examined the microstructure response of AA6061 alloy by uniaxial loading. In addition, the microstructure evolution mechanisms of AA6061 alloy subjected to cryogenic multidirectional forging and warm rolling were revealed by Rao et al. (Ref 18, 19). These results indicate a clear difference in the microstructures with increasing strain. Additionally, Hurley et al. (Ref 20) analyzed the influence of processing parameters on the grain structures of a 6061 alloy during hot rolling and developed recrystallization models.

According to previous studies (Ref 1, 4, 21-23), the constitutive model can be applied to simulate the flow behavior of the AA6061 alloy under UC. However, there is almost no attention devoted to the deformation behavior of the AA6061 alloy under PSC using a constitutive model and processing map. The processing map can be used to determine the optimum deformation parameters. Moreover, the reliability of the simulation results strongly depends on the constitutive model and deformation parameters. Thus, further studies are still required for a better understanding of these factors. In this study, a comparative study of the deformation behavior of an AA6061 alloy under UC and PSC was conducted on a Gleeble-

Fangcheng Qin, College of Materials Science and Engineering, Guilin University of Technology, Guilin, China; **Huiping Qi** and **Yongtang Li**, School of Materials Science and Engineering, Taiyuan University of Science and Technology, Taiyuan, China. Contact e-mails: qinfangcheng@glut.edu.cn and qhp9974@tyust.edu.cn.

3500 thermal simulator. The constitutive models were established, and the processing maps were developed. The optimum deformation parameters were obtained according to the processing maps and the observed microstructures. The results provide experimental evidence for hot ring rolling simulation in an AA6061 alloy.

2. Materials and Experimental Methods

The chemical composition of the AA6061 alloy used in this study is shown in Table 1. The AA6061 billet was produced by a continuous casting process. The homogenization heat treatment at 550 °C for 8 h was performed, and then the billet was slowly cooled to room temperature in air. The cylindrical specimens with a diameter of 10 mm and height of 15 mm were wire-cut from the as-cast billet for UC. The rectangular specimens with a length of 20 mm, width of 15 mm and height of 10 mm for PSC were also machined. Isothermal compression tests were conducted using UC and PSC techniques. The specimens were heated to 450 °C at a heating rate of 5 °C s^{-1} and soaked for 3 min. Subsequently, the specimens were cooled to the test temperatures at 5 °C s^{-1} and held for 1 min to eliminate the temperature gradient. The compression tests were carried out on a Gleeble-3500 thermal simulator at temperatures of 300 °C, 350 °C, 400 °C, 420 °C and 450 °C and strain rates of 0.01 s^{-1}, 0.1 s^{-1}, 1 s^{-1} and 5 s^{-1}. A tantalum sheet with a thickness of 0.1 mm and graphite foil lubricant were used to reduce the friction between the specimens and the anvils. The specimens were compressed to a true strain of approximately 0.9. After compression, the specimens were immediately quenched in water to room temperature to preserve the deformed microstructure. For the UC and PSC conditions, the load-stroke data measured in these tests were converted automatically into true stress-strain curves. To observe the microstructure, the compressed specimens were sectioned axially parallel to the compression axis and prepared for optical microscopy (OM, VHX-600E) by conventional methods, such as being ground, mechanically polished and etched by Keller's reagent. The average grain size was estimated using the method described in the ASTM E112 standard.

3. Results and Discussion

3.1 Initial Microstructure

Figure 1 presents the initial microstructure of the as-cast AA6061 alloy subjected to the homogenization heat treatment. The average grain size is approximately 75 μm. And some coarse second-phase particles are distributed along grain boundaries.

Table 1 Chemical composition of the AA6061 alloy (wt.%)

Si	Fe	Mg	Mn	Cu	Zn	Cr	Ti	Al
0.67	0.65	0.96	0.12	0.30	0.20	0.10	0.13	Balance

3.2 Flow Stress Behavior

The true stress-strain curves of the AA6061 alloy obtained from the PSC and the UC tests are shown in Fig. 2 and 3, respectively. It can be clearly seen that the stress increases dramatically to a peak value as the strain increases during the initial stage of deformation. Then, as the deformation exceeds the peak strain, the stress remains constant or decreases slightly to a certain value. Finally, it enters the steady-state stage, which is mainly attributed to work hardening and softening (Ref 24). It can also be seen that the stress increases with increasing strain rate at a constant temperature. The stress mainly depends on the DRV, and the dynamically recrystallized grains do not have enough time to fully accommodate at the high strain rate, and the softening effect cannot fully offset the hardening effect. Moreover, the stress decreases gradually with increasing temperature at a constant strain rate. This is simultaneously caused by the increase in the thermal activation and the decrease in the critical shear stress of crystal slip. The obstruction of the dislocation motion and the crystal slip is reduced. The softening effect gradually increases (Ref 25, 26). In addition, DRX is favorable for steady-state deformation by continuous stress softening and microstructure reconstitution (Ref 27). Thus, steady-state deformation is obtained because the competition between the hardening effect and softening effect reaches a dynamic balance. Moreover, a steady state usually results from the balance of the work hardening and DRV in aluminum alloys.

It is worth noting that the stress under PSC is slightly higher than that under UC under the same conditions. The stress-strain curves during PSC exhibit different characteristics. At lower strain rates ($\leq$ 1 s^{-1}), the stress in the PSC decreases monotonically after the peak strain. The temperature has a clear effect on the degree of stress softening. For example, the softening degree is approximately 20 MPa at 300 °C/0.01 s^{-1}, while it is only approximately 5 MPa at 450 °C/0.01 s^{-1}, as shown in Fig. 2(a). Under UC, the stress after the peak strain does not show obvious change across the accumulative strain. Moreover, the results show that at lower temperatures ($\leq$ 400 °C) and lower strain rates ($\leq$ 1 s^{-1}) under PSC, the AA6061 alloy presents high stress softening. Therefore, in
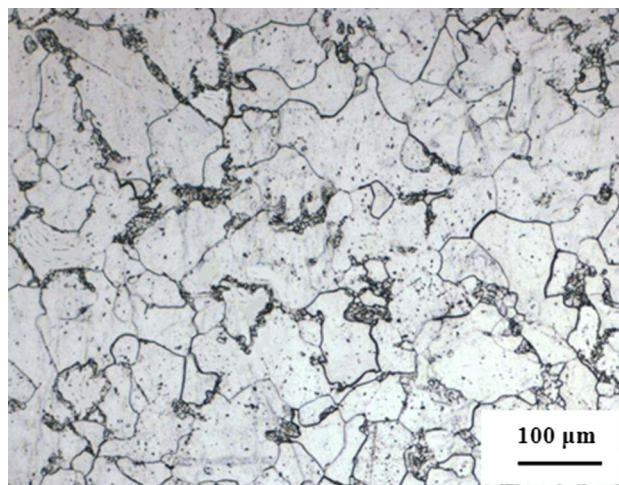

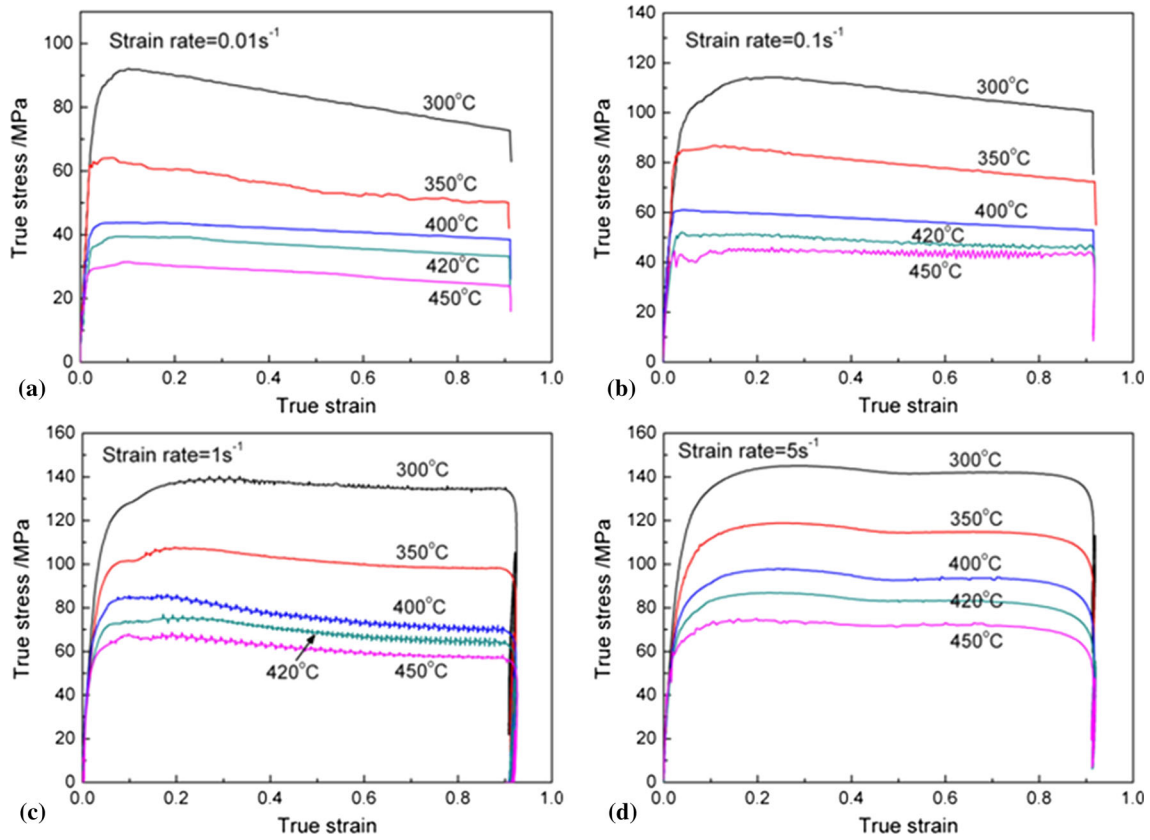**Fig. 1** Initial microstructure of the as-cast AA6061 alloy

Fig. 2 True stress-strain curves of AA6061 under PSC with strain rates of (a) 0.01 s^{-1}; (b) 0.1 s^{-1}; (c) 1 s^{-1}; and (d) 5 s^{-1}

this study, it was demonstrated that continuous stress softening behavior plays a dominant role in PSC.

3.3 Constitutive Analysis

The relationship among the flow stress, strain rate and temperature at a constant strain can be expressed as the hyperbolic sine-type equation proposed by Sellars and McTegart (Ref 28). The sensitivity of the stress to the temperature and strain rate can also be characterized by the Zener-Hollomon parameter (Z) based on the exponent-type equation (Ref 29-31):

$$Z = \dot{\varepsilon}\exp(Q/RT) = F_1(\sigma) = A_1\sigma^{n_1} \tag{Eq 1}$$

$$Z = F_2(\sigma) = A_2 \exp(\beta\sigma) \tag{Eq 2}$$

$$Z = F(\sigma) = A[\sinh(\alpha\sigma)]^n \tag{Eq 3}$$

where σ is the flow stress (MPa); $\dot{\varepsilon}$ is the strain rate (s^{-1}); Q is the apparent activation energy (kJ mol^{-1}); T is the absolute temperature (K); R is the universal gas constant (8.314 J mol^{-1} K^{-1}); A, A_1, A_2, β and α are material constants; n and n_1 are the stress exponents; and α can be calculated as $\alpha = \beta/n_1$.

The power law Eq 1 and exponent-type Eq 2 are suitable for a low stress level ($\alpha\sigma < 0.8$) and high stress level ($\alpha\sigma > 1.2$), respectively. Then, β and n_1 are taken as the average values of the slopes in the $\ln\dot{\varepsilon}$ versus σ plots and $\ln\dot{\varepsilon}$ versus $\ln\sigma$ plots, respectively, at a series of temperatures. The hyperbolic sine law, Eq 3, is a more general form suitable for all stress levels. Thus, the following relationship between the strain rate and stress can be obtained by substituting Eq 1 into Eq 3:

$$\dot{\varepsilon} = A \cdot [\sinh(\alpha\sigma)]^n \exp[-Q/RT] \tag{Eq 4}$$

To calculate the values of n and Q, the natural logarithm and partial differential of both sides of Eq 4 are taken as follows:

$$\ln\sinh(\alpha\sigma) = (1/n)\ln\dot{\varepsilon} + Q/(nRT) - (1/n)\ln A \tag{Eq 5}$$

$$Q = R\left[\frac{\partial\ln\dot{\varepsilon}}{\partial\ln[\sinh(\alpha\sigma)]}\right]_T\left[\frac{\partial\ln[\sinh(\alpha\sigma)]}{\partial(1/T)}\right]_{\dot{\varepsilon}} = RnS \tag{Eq 6}$$

The n and Q can be evaluated using Eq 5 and 6 and the true stress-strain data. The n is the average slope of $\ln\dot{\varepsilon}$ versus $\ln[\sinh(\alpha\sigma)]$ plots, and the S is the average slope of $\ln[\sinh(\alpha\sigma)]$ versus $(1/T)$ plots. In this study, the peak stresses are used to calculate the required material constants, and the detailed procedure is given below.

The plots to determine the average values of β, n_1, n and S for PSC and UC are presented in Fig. 4(a), (b), (c) and (d) and 5(a), (b), (c) and (d), respectively. Additionally, taking the natural logarithm of both sides of Eq 3, the value of A is expressed as:

$$\ln Z = \ln A + n\ln\sinh(\alpha\sigma) \tag{Eq 7}$$

By substitution of the $\ln Z$ values in Table 2 into Eq 7, the results are obtained and are given in Fig. 6. The material constants are listed in Table 3. Equation 8 and 9 is the constitutive models for the AA6061 alloy under PSC and UC with activation energies Q of 175.2 kJ mol^{-1} and 201.9 kJ mol^{-1}, respectively. It is well known that the activation energy is an important parameter for hot deformation and is closely related to the deformation mode except for the
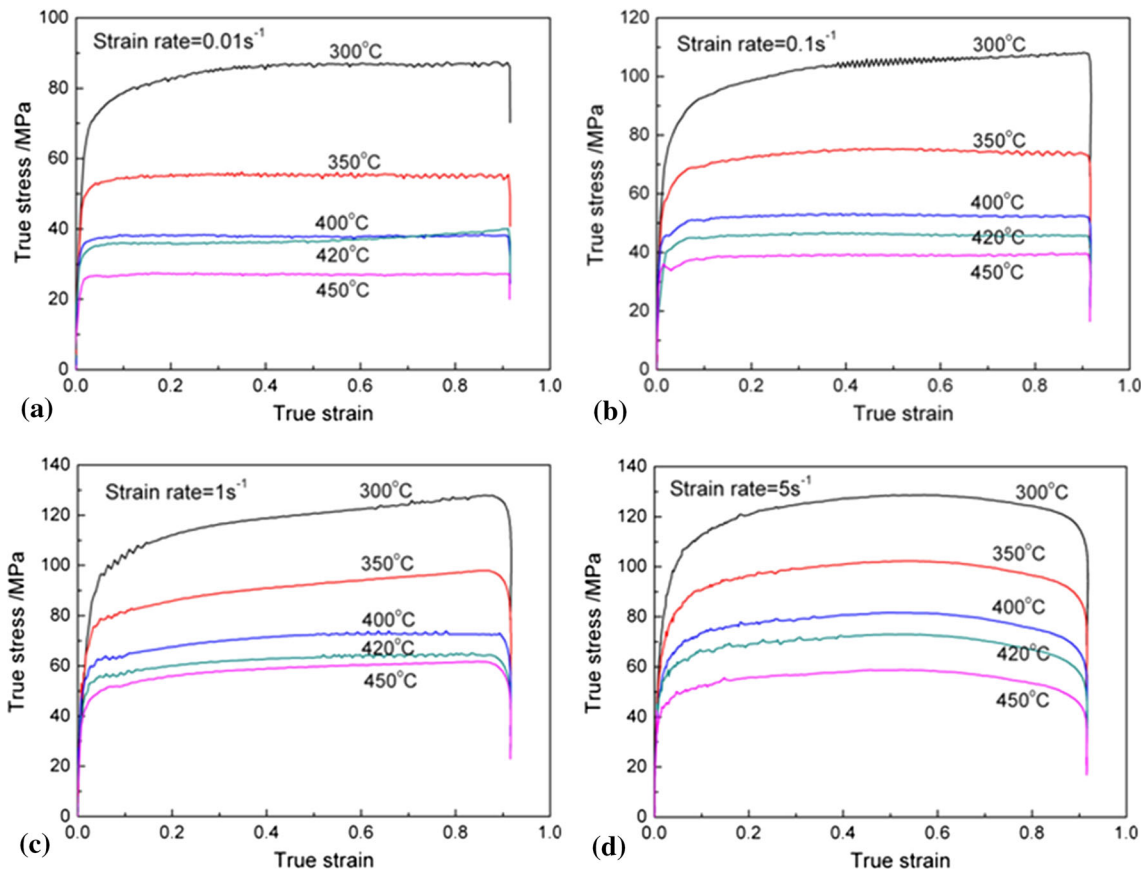
Fig. 3 True stress-strain curves of AA6061 under UC with strain rates of (a) 0.01 s^{-1}; (b) 0.1 s^{-1}; (c) 1 s^{-1}; and (d) 5 s^{-1}

alloy content and heat treatment (Ref 29, 32-34). In this study, the Q values for the AA6061 alloy under UC and PSC are lower than that for the solution heat-treated 6061 alloy (274 kJ mol^{-1}) (Ref 1), and higher than that for self-diffusion energy in pure aluminum (143 kJ mol^{-1}) (Ref 35, 36).

$$\dot{\varepsilon} = 7.06 \times 10^{12} \cdot [\sinh(0.01334\sigma)]^{6.4748} \exp[-175200/RT]$$

(Eq 8)

$$\dot{\varepsilon} = 8.51 \times 10^{14} \cdot [\sinh(0.01528\sigma)]^{6.8174} \exp[-201900/RT]$$

(Eq 9)

As shown in Table 3, the AA6061 alloy under PSC is characterized by a low activation energy, which strongly depends on the propagation of shear bands. Under UC, the maximum equivalent stress is concentrated in the center region of the specimen, as shown in Fig. 7(a). However, it is mainly concentrated at the side-edge between the rectangular specimen and anvils for PSC, as shown in Fig. 7(b). It is suspected that the maximum equivalent stress originated from the additional shear stress caused by the effect of the friction and tensile stress of the specimen under PSC (Ref 11). As the accumulated strain increases, the stress increases and further facilitates the propagation of shear bands. Additionally, as described by Cheng et al. (Ref 11), the shear bands in specimens under PSC are distinctly different from those under UC. The hardening rate can be reduced by the shear bands at low temperatures (≤ 400 °C) and low strain rates (≤ 1 s^{-1}). Therefore,

high stress softening is obtained, which results in a low activation energy during PSC.

As presented in Table 2 and Fig. 6, the Z parameter values of the AA6061 alloy during PSC and UC increase with increasing strain rate and decreasing temperature. Moreover, in Fig. 6, the correlation coefficient R for the regression analysis is greater than 0.99 and 0.98 during PSC and UC, respectively, which demonstrates that the developed constitutive models can provide a reliable estimate for the flow stress of the AA6061 alloy.

3.4 Processing Maps and Microstructure Evolution

Hot processing maps are helpful to optimize the deformation parameters for a wide range of metals and alloys. They have been widely used in the investigation of several mechanisms, such as DRV, DRX and flow instabilities (Ref 37, 38). Based on the dynamic materials model (DMM), the total power P consists of two complementary parts: the G content representing the power dissipated by plastic work and the J content related to the microstructure evolution. The total power is described as follows:

$$P = \sigma\dot{\varepsilon} = G + J = \int_0^{\dot{\varepsilon}} \sigma d\dot{\varepsilon} + \int_0^{\sigma} \dot{\varepsilon}d\sigma$$

(Eq 10)

where σ is the instantaneous flow stress and $\dot{\varepsilon}$ is the strain rate. The dissipated power J is calculated by:

$$J = \int_0^{\sigma} \dot{\varepsilon}d\sigma = \frac{m}{m+1} \sigma\dot{\varepsilon}$$
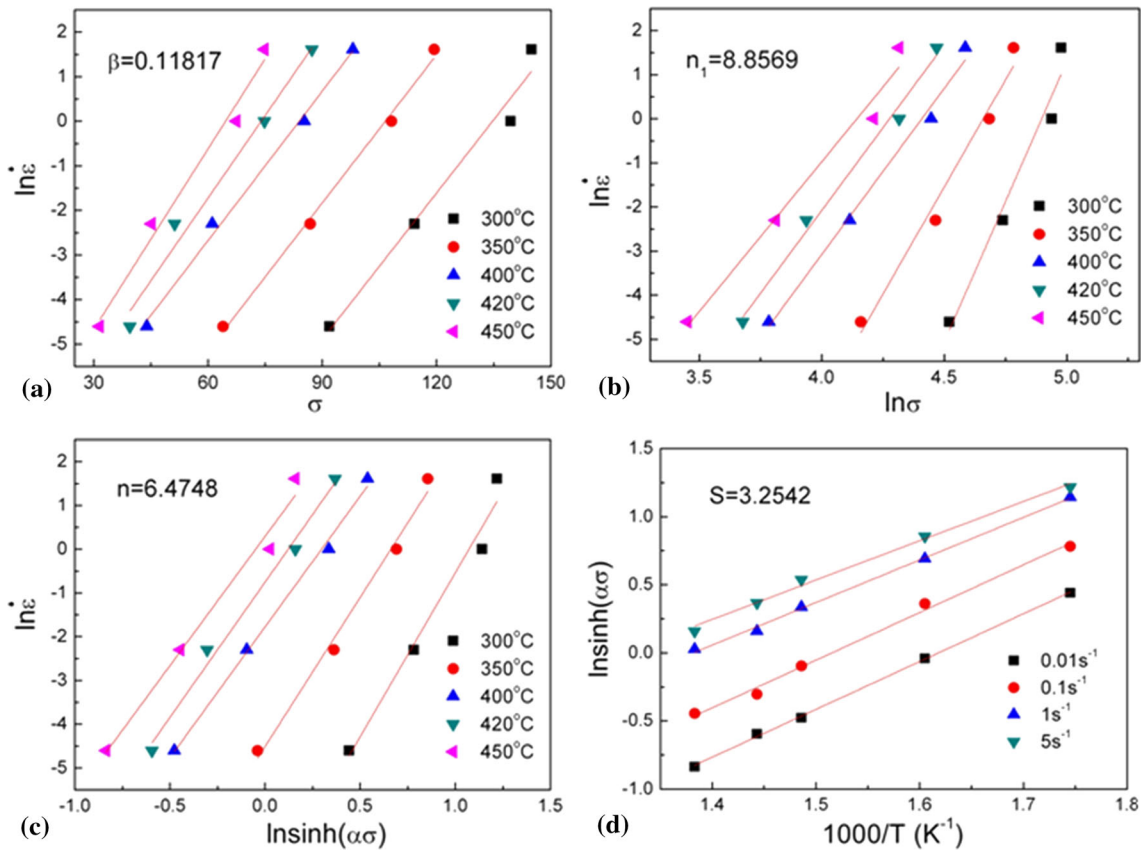
(Eq 11)

Fig. 4 Correlation between (a) $\ln\dot{\varepsilon} - \sigma$; (b) $\ln\dot{\varepsilon} - \ln\sigma$; (c) $\ln\dot{\varepsilon} - \ln[\sinh(\alpha\sigma)]$; (d) $\ln[\sinh(\alpha\sigma)] - (1000/T)$ for PSC

where m is the strain rate sensitivity. The value of J for a nonlinear dissipater is normalized with that of a linear dissipater ($m = 1$) to obtain the efficiency of the power dissipation and is given by:

$$m = \left(\frac{\mathrm{d}J}{\mathrm{d}G}\right)_{T,\varepsilon} = \left(\frac{\partial \ln\sigma}{\partial \ln\sigma\dot{\varepsilon}}\right)_{T,\varepsilon} \quad \text{(Eq 12)}$$

An efficiency of power dissipation (EPD) implies that the input power is dissipated by the microstructure evolution including the DRV, DRX and superplasticity. The rate of this change compared to an ideal linear dissipater is given by the dimensionless parameter (η) called the efficiency of power dissipation:

$$\eta = \frac{2m}{m+1}\Big|_{\varepsilon,T} \quad \text{(Eq 13)}$$

At a given strain, the variation of the EPD with the temperature and strain rate forms a map called a power dissipation map. In addition, an instability map is proposed based on the extremum principles of irreversible thermodynamics as applied to the continuum mechanics of a large plastic flow. The instability parameter ξ is described by (Ref 39-41):

$$\xi(\dot{\varepsilon}) = \frac{\partial \ln(m/m+1)}{\partial \ln\dot{\varepsilon}} + m \leq 0 \quad \text{(Eq 14)}$$

The instability map can be formed by the change in ξ with the temperature and strain rate, and the instability regions in this map can also be clarified by using the criterion $\xi \leq 0$. In regions with instability, microdefects involving flow localiza-

tion, adiabatic shear bands and crack propagation are predicted to occur during hot deformation. Thus, at a constant strain, the hot processing map can be developed by superimposing an instability map on a power dissipation map.

According to the above methods, the UC and PSC processing maps for the AA6061 alloy at a strain of 0.7 are presented in Fig. 8. The contour numbers show the EPD as a percentage, and the shaded areas represent the instability domains. From Fig. 8, it can be clearly seen that the EPD for the UC and PSC conditions varies with the temperature and strain rate. The map for the UC condition exhibits one region with a high EPD: in a temperature range of 360-450 °C and a strain rate range of 0.03-0.3 s^{-1}, with a peak EPD approximately 31% occurring at 450 °C/0.1 s^{-1}. For the PSC condition, three regions with a high EPD are identified. 1) One region is in a temperature range of 360-420 °C and a strain rate range of 1-5 s^{-1}, with a peak EPD approximately 33% occurring at 390 °C/5 s^{-1}. 2) The second region is in a temperature range of 430-450 °C and a strain rate range of 0.01-0.05 s^{-1}, with a peak EPD approximately 42% occurring at 450 °C/0.01 s^{-1}. 3) The third region is in a temperature range of 320-400 °C and a strain rate range of 0.01-0.05 s^{-1}, with a peak EPD approximately 35% at 370 °C/0.01 s^{-1}.

Previous research indicated that the EPD reflects the microstructure evolution, and the EPD values related to the DRV and DRX are 25-30% and 30-50%, respectively (Ref 42). Gandhi (Ref 43) concluded that DRV and DRX are beneficial processes because they can provide very considerably low stress and hardening rates. Thus, the intrinsic workability can be enhanced by eliminating microdefects and reconstituting the
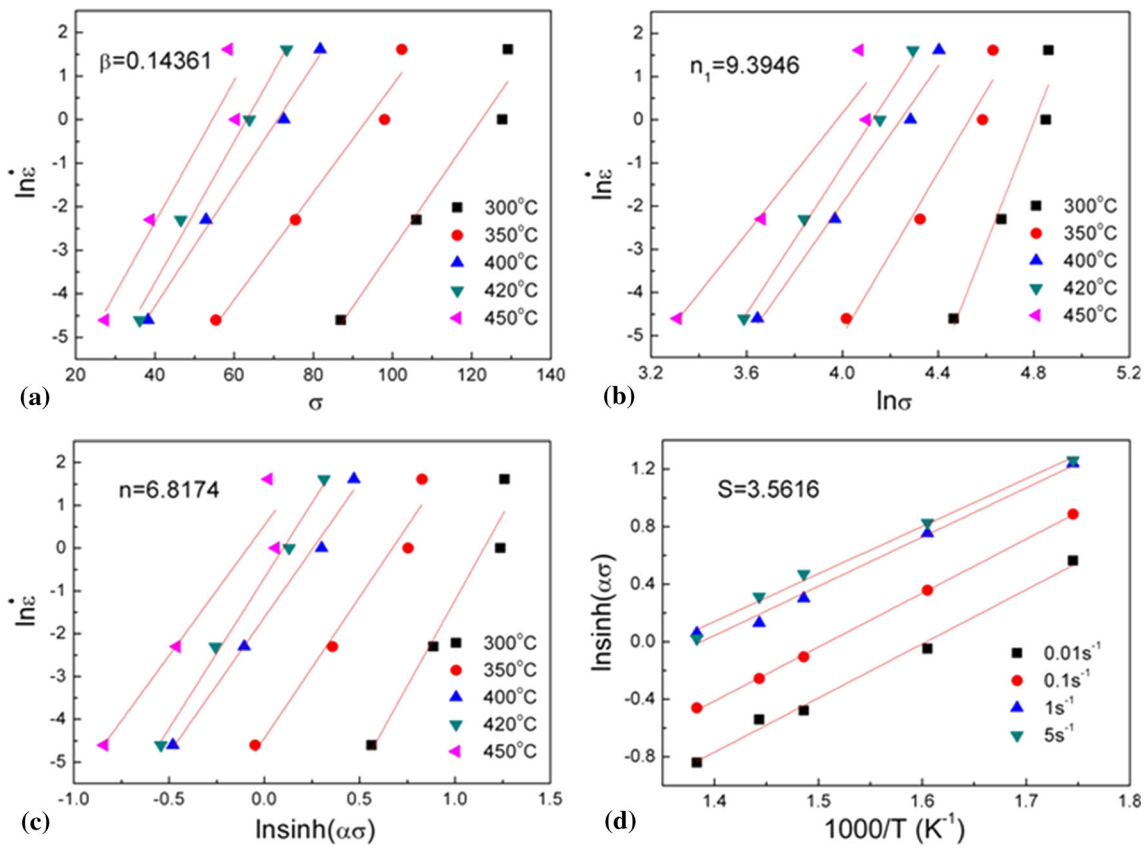
Fig. 5 Correlation between (a) $\ln\dot{\varepsilon} - \sigma$; (b) $\ln\dot{\varepsilon} - \ln\sigma$; (c) $\ln\dot{\varepsilon} - \ln[\sinh(\alpha\sigma)]$; (d) $\ln[\sinh(\alpha\sigma)] - (1000/T)$ for UC

Table 2 $\ln Z$ values of AA6061 alloy under PSC and UC (UC data shown in brackets)

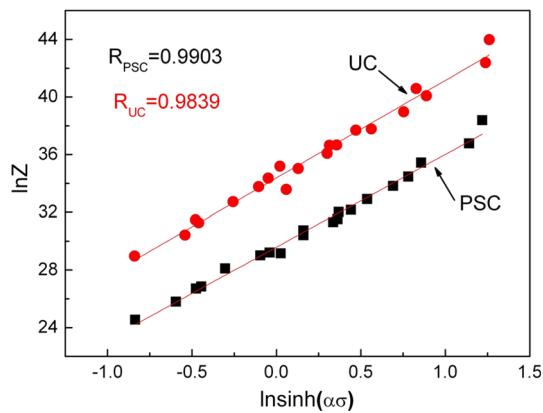| Strain rate, s^{-1}	Temperature, °C				
	300	350	400	420	450
0.01	32.16 (37.76)	29.21 (34.36)	26.70 (31.47)	25.79 (30.43)	24.53 (28.97)
0.1	34.46 (40.07)	31.51 (36.67)	29.01 (33.77)	28.10 (32.73)	26.84 (31.28)
1	36.77 (42.37)	33.82 (38.97)	31.31 (36.07)	30.41 (35.03)	29.14 (33.58)
5	38.38 (43.98)	35.43 (40.58)	32.91 (37.68)	32.01 (36.64)	30.75 (35.19)

Fig. 6 Correlation between $\ln Z$ and $\ln[\sinh(\alpha\sigma)]$

microstructure. Compared to the UC of the AA6061 alloy, the instability domain is relatively narrow during PSC, which occurs only at low temperatures (< 340 °C) and high strain rates (> 1 s^{-1}), as shown in Fig. 8(b).

Generally, the workability of metals and alloys tends to be improved by increasing the temperature and decreasing the strain rate (Ref 44). However, the low EPD presented in Fig. 8(a) implies a contrary result: The EPD of the AA6061 alloy under UC is lower than 18% in a temperature range of 400-450 °C and a strain rate range of 0.01-0.05 s^{-1}. This can be well explained by the observed microstructures; significant grain growth dominates at 420 °C/0.01 s^{-1} ($\ln Z = 30.43$). In Fig. 9(c), the average grain size is approximately 60 μm, and the coarse grains definitely deteriorate the workability of the AA6061 alloy. In the high-EPD domain (400 °C/0.1 s^{-1}), the grains are characterized by an elongated morphology and

Table 3 Values of material constants of AA6061 alloy under PSC and UC

Condition	A, s^{-1}	β	N_1	α, MPa^{-1}	N	Q, kJ mol^{-1}
PSC	7.06×10^{12}	0.11817	8.8569	0.01334	6.4748	175.2
UC	8.51×10^{14}	0.14361	9.3946	0.01528	6.8174	201.9
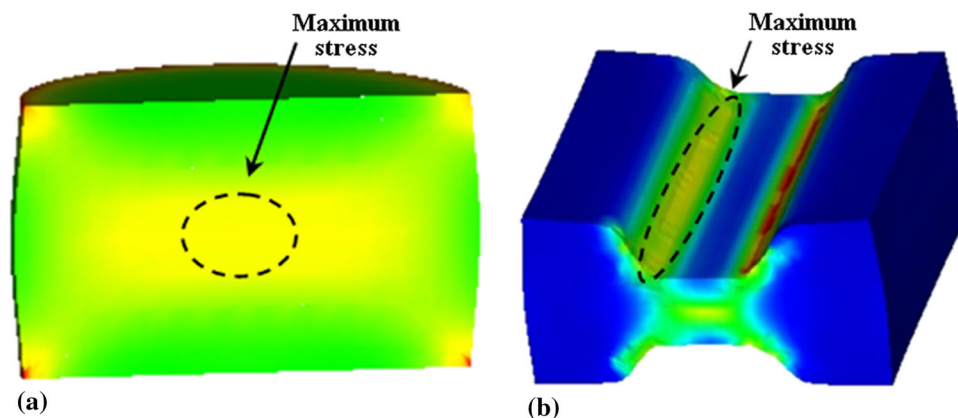
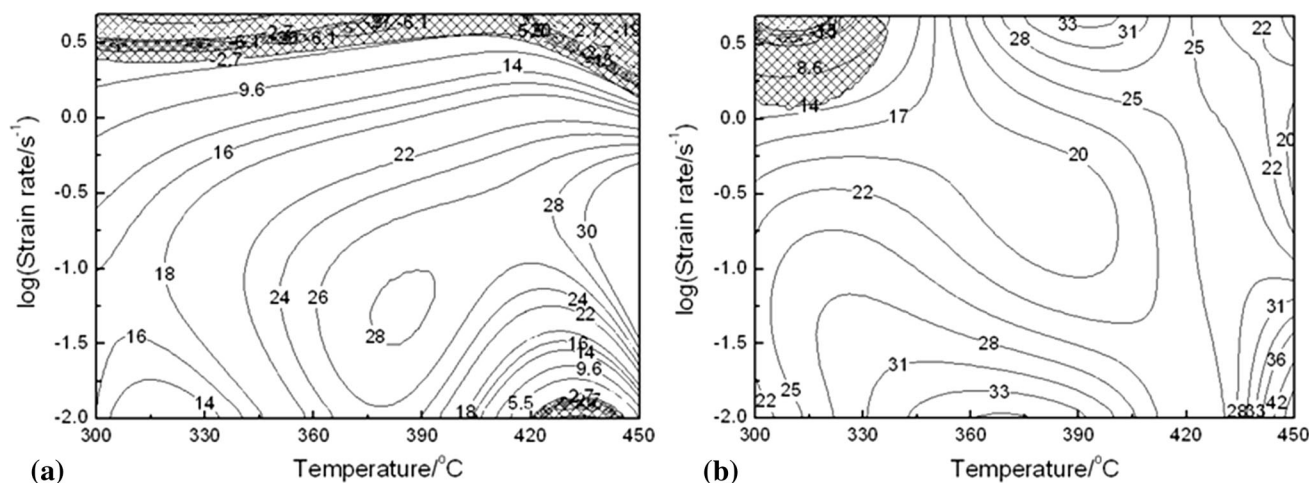**Fig. 7** Equivalent stress distribution of the AA6061 alloy during (a) UC and (b) PSC

Fig. 8 Processing maps of the AA6061 alloy at a strain of 0.7: (a) UC and (b) PSC conditions

subgrains, which are typical features of DRV (Figs. 9a and 10a). As the temperature increases, new recrystallization grains are observed, which demonstrate a slight DRX, as shown in Figs. 9(b) and 10(b) ($\ln Z = 31.28$). However, the subgrains can also be found in transgranular locations and boundaries under this condition. Subsequently, the size and volume fraction of the recrystallized grains increase. This is attributed to the combined effect of the temperature and strain rate on the recovery process. In Fig. 8(a), it can also be found that the EPD values for the DRV and DRX during UC are mainly between 28% and 31%, respectively. At 400 °C/5 s^{-1} ($\ln Z = 37.68$), an instability is caused because the insufficient deformation heat expanded from the center regions to the cooler areas of the specimens. The grains are distinctly elongated, as presented in Fig. 9(d). Thus, the softening mechanism in the AA6061 alloy after UC is the DRV, accompanied by slight DRX and grain

growth with a decrease in the Z value (shown in Table 2). Zhang et al. (Ref 45) also analyzed similar softening mechanisms during thermal deformation using isothermal compression tests.

In addition, the flow instability during PSC can also be seen in Fig. 11(d) by the high Z value. Compared to the AA6061 alloy under UC with a low strain rate of 0.1 s^{-1}, the DRV mechanism is clarified under PSC with a high strain rate of 5 s^{-1}. At 400 °C/5 s^{-1} ($\ln Z = 32.91$), the microstructure under PSC is mainly characterized by elongated grains and a large number of subgrains. The serrated boundaries are formed because of the preferred recovery in the vicinity of the grain boundaries, as shown in Fig. 11(a) and 12(a). The presence of the serrated boundaries is an indication of the occurrence of extended DRV (Ref 1). Thus, it can be concluded that the driving force is not high enough to cause DRX, resulting in
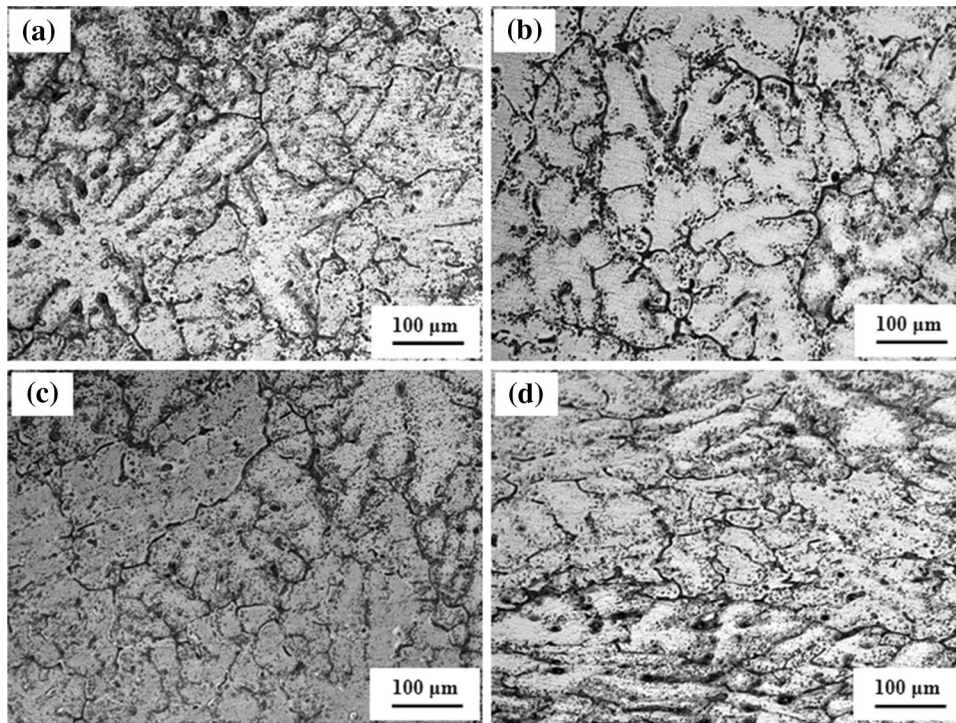
Fig. 9 Microstructures of the AA6061 alloy after UC under different conditions: (a) 400 °C/0.1 s^{-1} (lnZ = 33.77); (b) 450 °C/0.1 s^{-1} (lnZ = 31.28); (c) 420 °C/0.01 s^{-1} (lnZ = 30.43); and (d) 400 °C/5 s^{-1} (lnZ = 37.68)
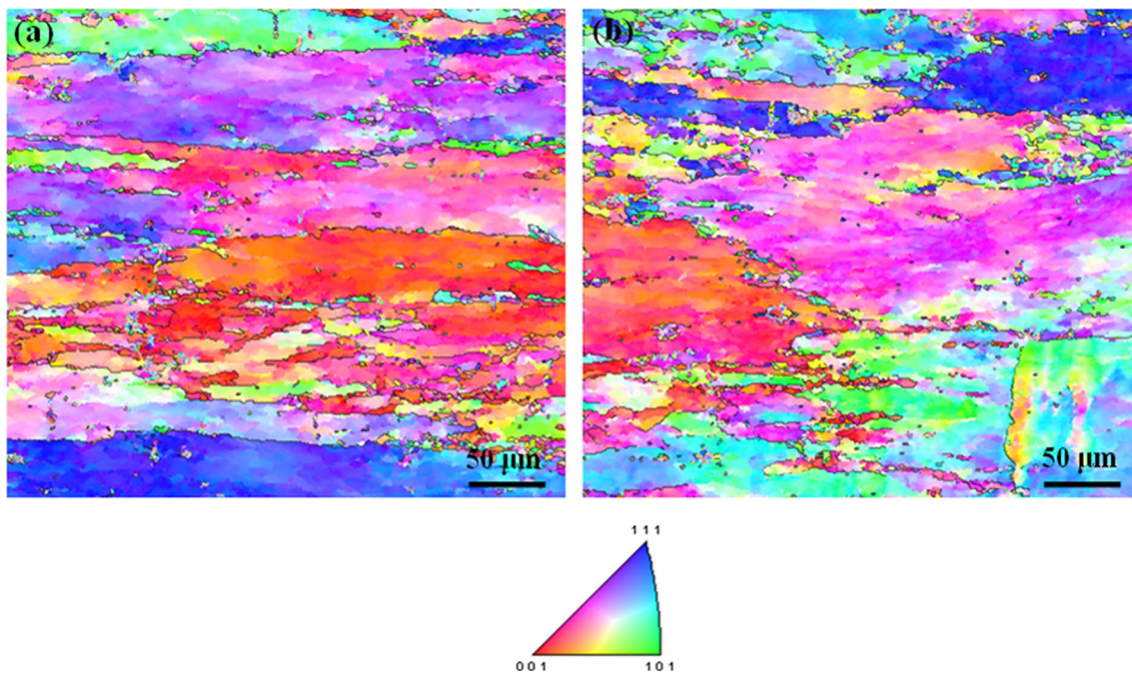

Fig. 10 EBSD maps of the AA6061 alloy after UC under different conditions: (a) 400 °C/0.1 s^{-1} (lnZ = 33.77) and (b) 450 °C/0.1 s^{-1} (lnZ = 31.28)

DRV. Additionally, recrystallized grains are observed at 350 °C/0.01 s^{-1} (lnZ = 29.21), and their average grain size and the DRX fraction increase as the temperature increases to 400 °C. In Fig. 11(b) and (c), the microstructures are characterized by elongated grains with the nucleation of new fine grains along boundaries. Moreover, the recrystallized grains are also shown in Fig. 11(c) and 12(b) with a low Z value. It can

also be found that the grain size increases and the subgrains decrease. Thus, as the Z value decreases, the DRX is enhanced under PSC compared with that under UC. However, the degree of DRX is still low during PSC. The softening mechanisms in the AA6061 alloy after PSC and UC are mainly due to DRV that is accompanied by a slight DRX. According to the developed processing maps and the microstructures, the
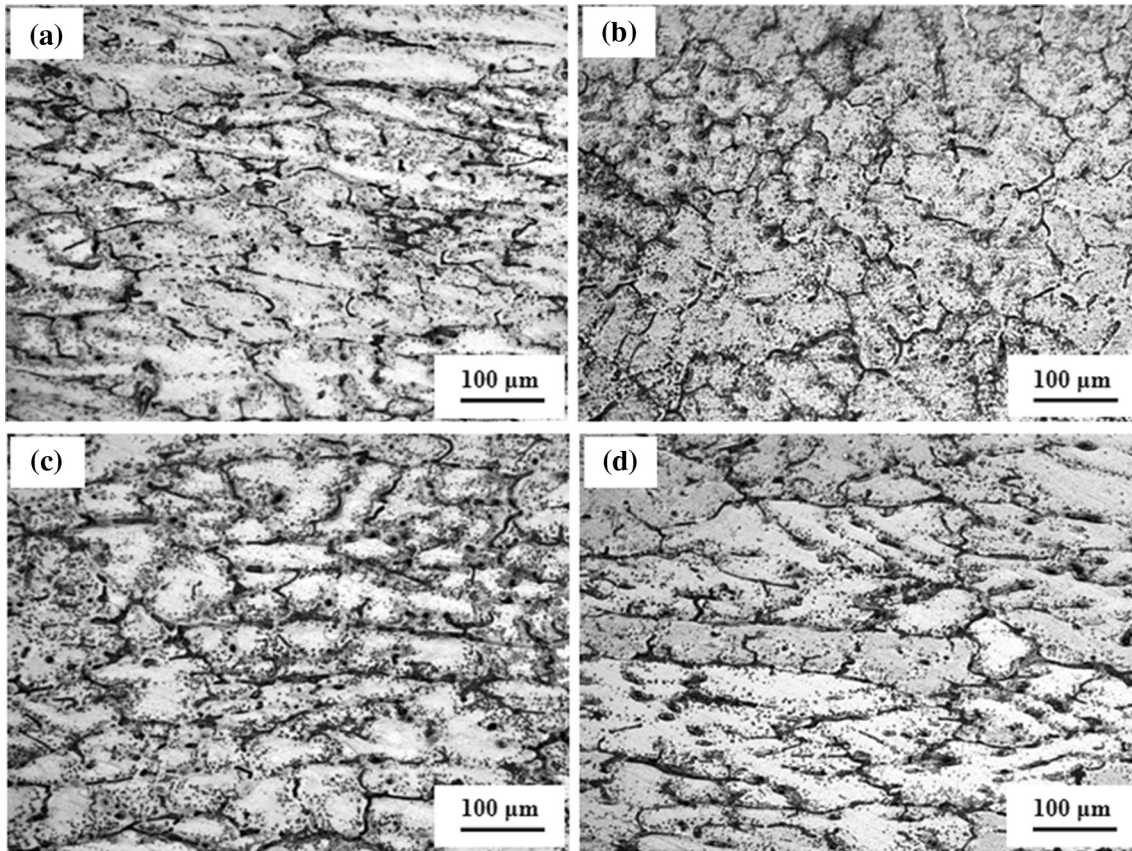
Fig. 11 Microstructures of the AA6061 alloy after PSC under different conditions: (a) 400 °C/5 s^{-1} (lnZ = 32.91); (b) 350 °C/0.01 s^{-1} (lnZ = 29.21); (c) 400 °C/0.01 s^{-1} (lnZ = 26.70); and (d) 300 °C/5 s^{-1} (lnZ = 38.38)
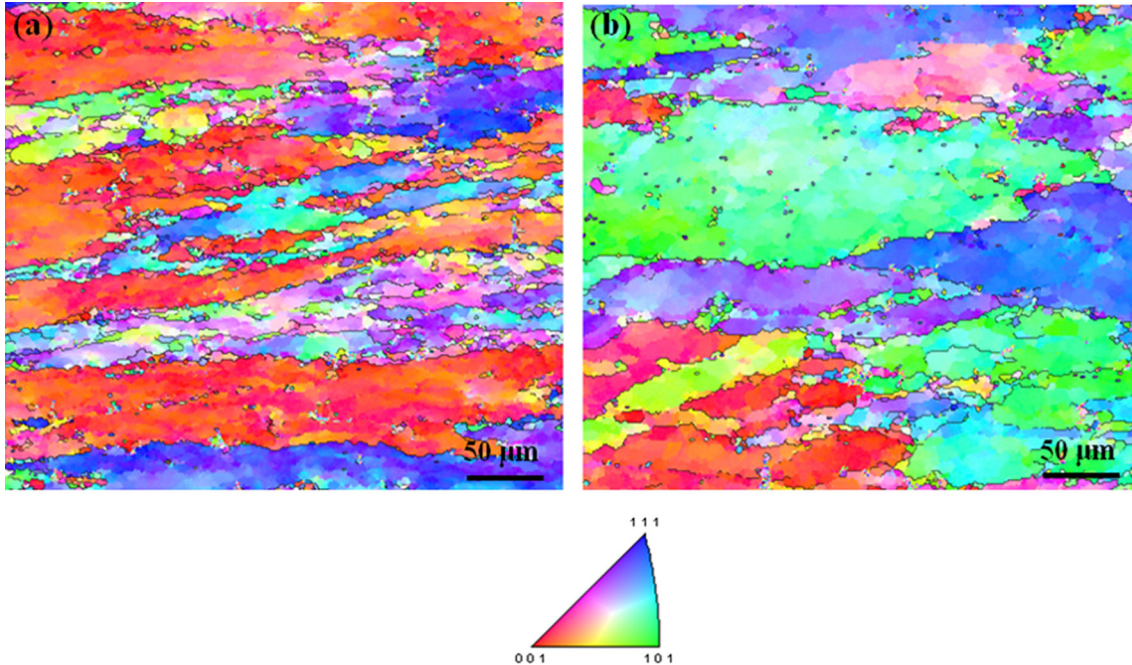

Fig. 12 EBSD maps of the AA6061 alloy after PSC under different conditions: (a) 400 °C/5 s^{-1} (lnZ = 32.91) and (b) 400 °C/0.01 s^{-1} (lnZ = 26.70)

optimum processing windows in a temperature range of 360-450 °C and a strain rate range of 0.03-0.3 s^{-1} with a peak EPD of 31% are suggested for the UC, and for the PSC, the temperature range of 320-400 °C and strain rate range of 0.01-0.05 s^{-1} with a peak EPD of 35% are recommended.

4. Conclusions

(1) Under the same deformation conditions, the flow stress under PSC is higher than that under UC. The constitutive models for PSC and UC can be represented by the Zener-Hollomon parameter (Z) in a hyperbolic sine-type equation with activation energies Q of 175.2 kJ mol^{-1} and 201.9 kJ/mol, respectively.

(2) Compared to that during UC, the instability domain of the AA6061 alloy is narrower during PSC. As the Z value decreases, the DRX tendency increases during PSC. The softening mechanisms in the AA6061 alloy after PSC and UC mainly involve the DRV accompanied by a slight DRX.

(3) The optimum parameters for UC include a temperature in the range of 360-450 °C and a strain rate in the range of 0.03-0.3 s^{-1} with a peak EPD of 31%, and for PSC, the optimum parameters include a temperature in the range of 320-400 °C and a strain rate in the range of 0.01-0.05 s^{-1} with a peak EPD of 35%.

References

1. H.R. Ezatpour, M.H. Sabzevar, S.A. Sajjadi, and Y.Z. Huang, Investigation of Work Softening Mechanisms and Texture in a Hot Deformed 6061 Aluminum Alloy at High Temperature, *Mater. Sci. Eng. A*, 2014, **606**, p 240–247

2. H.L. Yu, L.H. Su, C. Lu, K. Tieu, H.J. Li, J.T. Li, A. Godbole, and C. Kong, Enhanced Mechanical Properties of ARB-Processed Aluminum Alloy 6061 Sheets by Subsequent Asymmetric Cryorolling and Ageing, *Mater. Sci. Eng. A*, 2016, **674**, p 256–261

3. F. Ozturk, A. Sisman, S. Toros, S. Kilic, and R.C. Picu, Influence of Aging Treatment on Mechanical Properties of 6061 Aluminum Alloy, *Mater. Des.*, 2010, **31**, p 972–975

4. Y.H. Kim, T.K. Ryou, H.J. Choi, and B.B. Hwang, An Analysis of the Forging Processes for 6061 Aluminum-Alloy Wheels, *J. Mater. Process. Technol.*, 2002, **123**, p 270–276

5. W.S. Lee, J.C. Shyu, and S.T. Chiou, Effect of Strain Rate on Impact Response and Dislocation Substructure of 6061-T6 Aluminum Alloy, *Scripta Mater.*, 2000, **42**, p 51–56

6. U.M. Iqbal and V.S.S. Kumar, An Analysis On Effect of Multipass Twist Extrusion Process of AA6061 Alloy, *Mater. Des.*, 2013, **50**, p 946–953

7. N. Anjami and A. Basti, Investigation of Rolls Size Effects on Hot Ring Rolling Process by Coupled Thermo-Mechanical 3D-FEA, *J. Mater. Process. Technol.*, 2010, **210**, p 1364–1377

8. H. Yang, M. Wang, L.G. Guo, and Z.C. Sun, 3D Coupled Thermo-Mechanical FE Modeling of Blank Size Effects on the Uniformity of Strain and Temperature Distributions during Hot Rolling of Titanium Alloy Large Rings, *Comput. Mater. Sci.*, 2008, **44**, p 611–621

9. F.C. Qin, Y.T. Li, H.P. Qi, and L. Ju, Microstructure-Texture-Mechanical properties in Hot Rolling of A Centrifugal Casting Ring Blank, *J. Mater. Eng. Perform.*, 2016, **25**(3), p 1237–1248

10. K.H. Xu, W.X. Zhang, D.J. Yang, G.F. Zhang, Y.J. Li, and D. Liu, Manufacture of Aluminum Alloy 2219 Integral Ring with 9 m Ultra-Large Diameter, *Forg. Stamp. Technol.*, 2016, **41**(10), p 92–97 ((in Chinese))

11. S.L. Zhang, Y.M. He, and Z.Z. Li, Super Large Diameter Aluminium Alloy Ring Rolling Technology, *Ordnance Mater. Sci. Eng.*, 2007, **30**(5), p 58–59 ((in Chinese))

12. L. Cheng, X.Y. Xue, B. Tang, D.G. Liu, J.Z. Li, H.C. Kou, and J.S. Li, Deformation Behavior of Hot-Rolled IN718 Superalloy under Plane Strain Compression at Elevated Temperature, *Mater. Sci. Eng. A*, 2014, **606**, p 24–30

13. P. Uranga, I. Gutiérrez, and B. López, Determination of Recrystallization Kinetics from Plane Strain Compression Tests, *Mater. Sci. Eng. A*, 2013, **578**, p 174–180

14. D.W.A. Rees, Plane Strain Compression of Aluminium Alloy Sheets, *Mater. Des.*, 2012, **39**, p 495–503

15. T. Pettersen, B. Holmedal, and E. Nes, Microstructure Development during Hot Deformation of Aluminum to Large Strains, *Metall. Mater. Trans. A*, 2003, **34A**, p 2737–2744

16. T. Pettersen and E. Nes, Recrystallization of an AlMgSi Alloy after Different Modes of Hot Deformation, *Metall. Mater. Trans. A*, 2003, **34A**, p 2717–2726

17. A. Dorbane, G. Ayoub, B. Mansoor, R. Hamade, G. Kridli, and A. Imad, Observations of the Mechanical Response and Evolution of Damage of AA 6061-T6 under Different Strain Rates and Temperatures, *Mater. Sci. Eng. A*, 2015, **624**, p 239–249

18. P.N. Rao, D. Singh, and R. Jayaganthan, Mechanical Properties and Microstructural Evolution of Al6061 Alloy Processed by Multidirectional Forging at Liquid Nitrogen Temperature, *Mater. Des.*, 2014, **56**, p 97–104

19. P.N. Rao and R. Jayaganthan, Effects of Warm Rolling and Ageing after Cryogenic Rolling on Mechanical Properties and Microstructure of Al 6061 Alloy, *Mater. Des.*, 2012, **39**, p 226–233

20. N.D. Hurley, W.H.V. Geertruyden, and W.Z. Misiolek, Surface Grain Structure Evolution in Hot Rolling of 6061 Aluminum Alloy, *J. Mater. Process. Technol.*, 2009, **209**, p 5990–5995

21. J. Ding, G.Z. Kang, Q.H. Kan, and Y.J. Liu, Constitutive Model for Uniaxial Time-Dependent Ratcheting of 6061-T6 Aluminum Alloy, *Comput. Mater. Sci.*, 2012, **57**, p 67–72

22. Q.L. Jin, Experimental Study on Hot Deformation Behavior and Microstructure Evolution of Aluminum Alloy 6061, *Trans. Mater. Heat Treatment*, 2011, **32**(6), p 51–57 ((in Chinese))

23. F.J. Li, Y.W. Zhai, Y. Bian, and Z.P. Zhong, Study of Plastic Deformation Behavior on 6061 Aluminum Alloy, *J. Plast. Eng.*, 2015, **22**(2), p 95–99 ((in Chinese))

24. Y. Zhang, S. Jiang, Y. Zhao, and D. Shan, Isothermal Precision Forging of Complex-Shape Rotating Disk of Aluminum Alloy Based on Processing Map and Digitized Technology, *Mater. Sci. Eng. A*, 2013, **580**, p 294–304

25. Y.C. Lin, F.Q. Nong, X.M. Chen, D.D. Chen, and M.S. Chen, Microstructural Evolution and Constitutive Models to Predict Hot Deformation Behaviors of A Nickel-Based Superalloy, *Vacuum*, 2017, **137**, p 104–114

26. D.D. Chen, Y.C. Lin, Y. Zhou, M.S. Chen, and D.X. Wen, Dislocation Substructures Evolution and An Adaptive-Network-Based Fuzzy Inference System Model for Constitutive Behavior of A Ni-Based Superalloy during Hot Deformation, *J. Alloys Compd.*, 2017, **708**, p 938–946

27. Q.F. Qin, Y.X. Tan, Z.M. Zhang, Q. Wang, and Y.B. Yang, Effects of Homogenization on Hot Deformation Behavior of As-Cast Mg-8Gd-3Y-1Nd-0.5Zr Magnesium Alloy, *J. Mater. Eng. Perform.*, 2016, **25**(1), p 304–311

28. C.M. Sellars and W.J. McTegart, On the Mechanism of Hot Deformation, *Acta Metall.*, 1966, **14**, p 1136–1138

29. E. Cerri, E. Evangelista, A. Forcellese, and H.J. McQueen, Comparative Hot Workability of 7012 and 7075 Alloys after Different Pretreatments, *Mater. Sci. Eng. A*, 1995, **197**, p 181–198

30. D.G. He, Y.C. Lin, M.S. Chen, J. Chen, D.X. Wen, and X.M. Chen, Effect of Pre-treatment on Hot Deformation Behavior and Processing

Map of an Aged Nickel-based Superalloy, *J. Alloys Compd.*, 2015, **649**, p 1075–1084

31. Y.X. Liu, Y.C. Lin, and Y. Zhou, 2D Cellular Automaton Simulation of Hot Deformation Behavior in A Ni-Based Superalloy under Varying Thermal-Mechanical Conditions, *Mater. Sci. Eng. A*, 2017, **691**, p 88–99

32. S.Y. Chen, K.H. Chen, G.S. Peng, X.H. Chen, and Q.H. Ceng, Effect of Heat Treatment on Hot Deformation Behavior and Microstructure Evolution of 7085 Aluminum Alloy, *J. Alloys Compd.*, 2012, **537**, p 338–345

33. S.D. Liu, J.H. You, X.M. Zhang, Y.L. Deng, and Y.B. Yuan, Influence of Cooling Rate after Homogenization on the Flow Behavior of Aluminum Alloy 7050 under Hot Compression, *Mater. Sci. Eng. A*, 2010, **527**, p 1200–1205

34. J. Zhang, B.Q. Chen, and B.X. Zhang, Effect of Initial Microstructure on the Hot Compression Deformation Behavior of A 2219 Aluminum Alloy, *Mater. Des.*, 2012, **34**, p 15–21

35. W.A. Soer, A.R. Chezan, and J.T.M. De Hosson, Deformation and Reconstruction Mechanisms in Coarse-Grained Superplastic Al-Mg Alloys, *Acta Mater.*, 2006, **54**, p 3827–3833

36. Y.B. Yang, Z.P. Xie, Z.M. Zhang, X.B. Li, Q. Wang, and Y.H. Zhang, Processing Maps for Hot Deformation of the Extruded 7075 Aluminum Alloy Bar: Anisotropy of Hot Workability, *Mater. Sci. Eng., A*, 2014, **615**, p 183–190

37. Y.V.R.K. Prasad, H.L. Gegel, and S.M. Doraivelu, Modeling of Dynamic Material Behavior in Hot Deformation: Forging of Ti-6242, *Metall. Mater. Trans. A*, 1984, **15**, p 1883–1892

38. P.S. Robi and U.S. Dixit, Application of Neural Networks in Generating Processing Map for Hot Working, *J. Mater. Process. Technol.*, 2003, **142**, p 289–294

39. Y.V.R.K. Prasad and K.P. Rao, Mechanisms of High Temperature Deformation in Electrolytic Copper in Extended Ranges of Temperature and Strain Rate, *Mater. Sci. Eng. A*, 2004, **374**, p 335–341

40. K.P. Rao, Y.V.R.K. Prasad, K. Suresha, N. Hort, and K.U. Kainer, Hot Deformation Behavior of Mg-2Sn-2Ca Alloy in As-Cast Condition and after Homogenization, *Mater. Sci. Eng. A*, 2012, **552**, p 444–450

41. D.X. Wen, Y.C. Lin, H.B. Li, X.M. Chen, J. Deng, and L.T. Li, Hot Deformation Behavior and Processing Map of a Typical Ni-based Superalloy, *Mater. Sci. Eng. A*, 2014, **591**, p 183–192

42. M.J. Zhang, F.G. Li, S.Y. Wang, and C.Y. Liu, Characterization of Hot Deformation Behavior of A P/M Nickel-Base Superalloy using Processing Map and Activation Energy, *Mater. Sci. Eng. A*, 2010, **527**, p 6771–6779

43. C. Gandhi, On Fracture Initiation Mechanisms and Dynamic Recrystallization during Hot Deformation of Pure Nickel, *Metall. Trans. A*, 1982, **13**(7), p 1233–1238

44. L. Chen, G.Q. Zhao, J. Gong, X.X. Chen, and M.M. Chen, Hot Deformation Behaviors and Processing Maps of 2024 Aluminum Alloy in As-Cast and Homogenized States, *J. Mater. Eng. Perform.*, 2015, **24**, p 5002–5012

45. X.H. Zhang, Y. Zhang, B.H. Tian, Y.L. Jia, Y. Liu, K.X. Song, and A.A. Volinsky, Thermal Deformation Behavior of the Al2O3-Cu/(W, Cr) Electrical Contacts, *Vacuum*, 2019, **164**, p 361–366